organic material in any unit below unit 1, and (v) the lack of evidence of vegetation growth except locally within units 2 and 3. Because intense precipitation along the arid Peruvian coast is typically associated with El Niño events today, we infer that such events also produced the debris-flow and flood deposits at Quebrada Tacahuay.

Radiocarbon dating of units 1, 2, 3, 4, 4c3, and 8 (Table 1 and Fig. 2) divide the sedimentary history of the site after deposition of unit 8 into three periods. First, between about 12,500 and 8900 to 8700 cal. yr B.P., four extensive debris flows (units 2, 3, 6, and 7) and an extensive sheetflood (unit 4) covered the site—an average of one sedimentation event every 700 to 800 years. In contrast, between about 8900 to 8700 and about 5300 cal. yr B.P., the only flood or debris-flow sediments deposited were two thin and fine-grained debris-flow units confined to a small channel and exposed in only one profile (units 4c1 and 4c2, Fig. 2). Flood and debris-flow activity thus diminished significantly in both severity and frequency during this period, which corresponds to the ~8900 to 5700 cal. yr B.P. (8000 to 5000 ^{14}C yr B.P.) hiatus in El Niño activity deduced from shell-midden data farther north (12). Finally, at ~5300 cal. yr B.P., another extensive debris-flow deposit (unit 1) covered the site at Quebrada Tacahuay before sediment supply was cut off by incision of the present main channel (Fig. 1). The debris-flow and flood deposits underlying unit 8 have not been dated but are older than the ~12,700 to 12,500 cal. yr B.P. age of that unit. The similarities between them and the younger sediments suggest that conditions producing El Niño events were also present there in the Pleistocene.

The Quebrada Tacahuay site was almost certainly used largely or entirely for obtaining maritime resources as indicated by the overwhelming proportion of maritime elements (99.8%) in the faunal remains. Indications that most or all of these remains were associated with anthropogenic activity include evidence of butchering, the large numbers of burned bones, the presence of marine mollusk fragments, and the spatial association of the remains with the hearth and lithic artifacts. The primary activity at the site evidently was processing seabirds, and secondary activities included processing fish and shellfish. We therefore infer that people with a maritime-based economy were present there about 12,700 to 12,500 years ago, during the period when the Andean coast was first settled. After that time, catastrophic floods and debris flows may have affected the occupation history of the site. A debris flow inundated the site, possibly when it was still in use, and the locality was not reoccupied until ~3500 years later, when flood and debris-flow activity had substantially diminished.

References and Notes

1. M. Aldenderfer, *Quat. Int.*, in press.
2. C. Chauchat, in *Peruvian Prehistory*, R. W. Keatinge, Ed. (Cambridge Univ. Press, Cambridge, 1988), pp. 41–66.
3. J. B. Richardson III, in *Early Man in America*, A. L. Bryan, Ed. (Archaeological Researches International, Edmonton, Alberta, 1978), pp. 274–289; *Rev. Arqueología Am.* **6**, 71 (1992).
4. P. P. Ossa, in *Early Man in America*, A. L. Bryan, Ed. (Archaeological Researches International, Edmonton, Alberta, 1978), pp. 290–295; C. Chauchat, *Préhistoire de la Côte Nord du Pérou* (Cahiers du Quaternaire, no. 18, CNRS, Paris, 1992).
5. D. H. Sandweiss, J. B. Richardson III, E. J. Reitz, J. T. Hsu, R. A. Feldman, in *Ecology, Settlement, and History in the Osmore Drainage, Peru*, D. S. Rice, C. Stanish, P. R. Scarr, Eds. (Br. Archaeol. Rep. Int. Ser. 545i, 1989), pp. 35–84.
6. A. C. Roosevelt *et al.*, *Science* **272**, 373 (1996); R. E. Taylor, C. V. Haynes Jr., M. Stuiver, *Antiquity* **70**, 515 (1996).
7. For recent discussions, see papers presented at Society for American Archaeology's 63rd Annual Meeting Symposium on Terminal Pleistocene/Early Holocene Maritime Adaptations Along the Pacific Coast of the Americas, 27 March 1998, Seattle, WA.
8. M. E. Moseley, *The Maritime Foundations of Andean Civilization* (Cummings, Menlo Park, CA, 1975); *Andean Past* **3**, 5 (1992).
9. D. H. Sandweiss *et al.*, *Science* **281**, 1830 (1998).
10. See, for example, C. N. Caviedes, *Geogr. Rev.* **74**, 267 (1984).
11. L. E. Wells, *J. Geophys. Res.* **92**, 14463 (1987); thesis, Stanford University, Stanford, CA (1988); *Geology* **18**, 1134 (1990); L. Ortlieb, T. J. DeVries, A. Díaz, *Bol. Soc. Geol. Perú* **81**, 127 (1990); A. Díaz and L. Ortlieb, *Bull. Inst. Fr. Et. Andines* **22**, 159 (1993); L. Ortlieb and J. Macharé, *Global Planet. Change* **7**, 181 (1993); L. Ortlieb, A. Díaz, N. Guzman, *Quat. Sci. Rev.* **15**, 857 (1996); T. J. DeVries, L. Ortlieb, A. Díaz, L. E. Wells, C. Hillaire-Marcel, *Science* **276**, 965 (1997); L. E. Wells and J. S. Noller, *ibid.*, p. 966.
12. D. H. Sandweiss, J. B. Richardson III, E. J. Reitz, H. B. Rollins, K. A. Maasch, *Science* **273**, 1531 (1996); *ibid.* **276**, 966 (1997).
13. E. Bard *et al.*, *Nature* **382**, 241 (1996).
14. The marine mollusk fragments are almost certainly of anthropogenic origin, as evidenced by their terrestrial location and context. Fish remains may be transported in the digestive systems of seabirds [D. G. Ainley, D. W. Anderson, P. R. Kelley, *Condor* **83**, 120 (1981); D. C. Duffy and L. J. B. Laurenson, *ibid.* **85**, 305 (1983)], but the burned anchovy remains in the hearth and the lack of any evidence of digestive changes from stomach acids indicate that the fish remains are also of anthropogenic origin.
15. The following skeletal elements contain butchering evidence: *Sula* spp. (booby)—one furcula, two coracoids, one scapula, one ulna; *Pelecanus* sp. (pelican)—one digit; *Phalacrocorax bougainvillii* (guanay cormorant)—one scapula, three humeri; *Phalacrocorax* spp. (cormorant)—one furcula, one coracoid, one radius, one ulna; Aves unidentified—one rib, one radius, two shaft fragments.
16. One artifact (31b, Fig. 1) was on the deflated sand surface of unit 8, under an overhang. The other (31a, Fig. 1) was on the surface immediately below the contact between units 8 and 9, partly covered by a thin layer of slope wash.
17. M. Stuiver and P. J. Reimer, *Radiocarbon* **35**, 215 (1993).
18. We thank J. Alley, M. E. Moseley, and P. R. Williams for assistance in the field; the Asociación Contisuyo del Perú for logistical and financial support; the Florida Museum of Natural History for access to comparative skeletal collections; and K. R. Lajoie, D. H. Sandweiss, D. W. Steadman, and L. E. Wells for comments.

4 June 1998; accepted 31 July 1998

Turbulent Transport Reduction by Zonal Flows: Massively Parallel Simulations

Z. Lin,* T. S. Hahm, W. W. Lee, W. M. Tang, R. B. White

Three-dimensional gyrokinetic simulations of microturbulence in magnetically confined toroidal plasmas with massively parallel computers showed that, with linear flow damping, an asymptotic residual flow develops in agreement with analytic calculations. Nonlinear global simulations of instabilities driven by temperature gradients in the ion component of the plasma support the view that turbulence-driven fluctuating zonal flows can substantially reduce turbulent transport. Finally, the outstanding differences in the flow dynamics observed in global and local simulations are found to be due to profile variations.

Turbulence shear suppression by $\mathbf{E} \times \mathbf{B}$ flows (plasma flows induced by an electric field perpendicular to a magnetic field line) is the most likely mechanism responsible for the transition to various forms of enhanced confinement regimes observed in magnetically confined plasmas (1). Understanding the mechanisms of turbulence suppression (2, 3) and developing techniques to control turbulence are needed for developing magnetic fusion. Recent experimental data from tokamaks (4) revealed the presence of small radial-scale $\mathbf{E} \times \mathbf{B}$ flows that cannot be explained by the existing neoclassical (Coulomb collisional) theory. These observations point to the possibility that $\mathbf{E} \times \mathbf{B}$ zonal flows generate spontaneously and regulate the turbulence. Turbulent transport is believed to arise from electrostatic pressure-gradient–driven instabilities. These highly complex nonlinear phenomena can be most effectively investigated by numerical experiments. One of the most promising approaches is gyrokinetic particle-in-cell simulation (5), which suppress-

Princeton Plasma Physics Laboratory, Princeton University, Post Office Box 451, Princeton, NJ 08543, USA.

es the rapid gyromotion of a charged particle about the magnetic field line. By use of low-noise numerical algorithms (6, 7) and massively parallel computers, we were able to reproduce key features of turbulent transport observed at the core of tokamak plasmas.

Previous toroidal gyrokinetic and gyrofluid (8) simulations of instabilities driven by the ion-temperature gradient (ITG) in a local geometry, which follows a magnetic field line (8–10), have indicated that turbulence-driven zonal flows play a crucial role in regulating nonlinear saturation and transport levels. However, global gyrokinetic simulations, which treat the whole plasma volume, either did not include (11) or did not observe (12, 13) substantial effects of these self-generated flows in steady-state transport. Because local simulations are restricted to a flux-tube domain of a few turbulence decorrelation lengths with radially periodic boundary conditions and assume scale separation between the turbulence and equilibrium profiles, the key issues of transport scaling and effects of steep pressure profiles in transport barriers can be most effectively studied in global simulations.

We developed a fully three-dimensional (3D) global gyrokinetic toroidal code (GTC) (7) based on the low-noise nonlinear δf scheme (6) for studying both turbulence and neoclassical physics. The code uses a general geometry Poisson solver (14) and Hamiltonian guiding center equations of motion (15) in magnetic coordinates (16) to treat both advanced axisymmetric and nonaxisymmetric configurations with realistic numerical magnetohydrodynamics equilibria. This global code takes into account equilibrium profile variation effects and has low particle noise. Furthermore, a single code can simulate both a full poloidal cross section and an annular box to provide a connection between global and local simulations. The GTC code was implemented as a platform-independent program and achieved nearly perfect scalability on various massively parallel processing (MPP) systems (for example, CRAY-T3E

and Origin-2000 supercomputers). This scalability enables us to fully use the rapidly increasing MPP computer power that presently allows routine nonlinear simulations of more than 10^8 particles to treat realistic plasmas parameters of existing fusion experiments. Nevertheless, a more than two orders of magnitude increase in computing power will be required to assess turbulent transport properties of reactor-relevant plasmas with additional key features such as nonadiabatic electron response, electromagnetic perturbations, and larger system size.

The GTC code was benchmarked against earlier analytic and computational models for neoclassical transport (17) and toroidal ITG simulations (7). Linear ITG growth rates and real frequencies agree well with results from linear gyrofluid code (8) calculations, and steady-state transport results are consistent with those from global gyrokinetic Cartesian code (11) nonlinear simulations when turbulence-driven $\mathbf{E} \times \mathbf{B}$ flows are suppressed. We tested convergence by varying the size of each time step, the number of grid points, and the number of particles in nonlinear simulations. The convergence of the ion heat conductivity χ_i and fluctuation energy level with respect to the number of particles was demonstrated in nonlinear simulations with 20 million grid points with representative plasma parameters from tokamak experiments. The ion heat conductivity remained unchanged when the number of particles was increased from 32 million to 80 million. Similar convergence of the fluctuation energy was obtained with 80 million particles.

Turbulence-generated zonal flows in toroidal plasmas are driven by the flux-surface–averaged radially local charge separation and mainly in the poloidal direction for high–aspect ratio devices. Rosenbluth and Hinton (18)

showed that an accurate prediction of the undamped component of poloidal flows is important in determining the transport level in nonlinear turbulence simulations and provided an analytical test for predicting the residual flow level in response to an initial flow perturbation. We reproduced this test in gyrokinetic particle simulations by solving the toroidal gyrokinetic equation (19) with an initial source that is constant on a flux surface and introduced a perturbation of the poloidal flow. This flow was relaxed through the transit time magnetic pumping effect (20) followed by a slower damped oscillation with a characteristic frequency corresponding to that of the geodesic acoustic mode (21). The residual level of this flow measured from the simulation agrees well with the theoretical prediction (18).

Turbulence-driven zonal flows are now self-consistently included in the nonlinear simulations of toroidal ITG instabilities. The flows are generated by the Reynolds stress (22) and can be considered as a nonlinear instability associated with inverse cascade of the turbulent spectra (23). Our global simulations produced fluctuating $\mathbf{E} \times \mathbf{B}$ zonal flows containing substantial components with radial scales and frequencies comparable to those of the turbulence. These results are in qualitative agreement with flux-tube simulations (8, 10) and demonstrate the possible existence and the importance of such fluctuating flows. These simulations used representative parameters of DIII-D tokamak high confinement mode core plasmas, which have a peak ion-temperature gradient at minor radius $r = 0.5a$ with the following local parameters: $R_0/L_T = 6.9$, $L_n/L_T = 3.2$, $q = 1.4$, $(r/q)(dq/dr) = 0.78$, $T_e/T_i = 1$, and $a/R_0 = 0.36$, where R_0 is the major radius, L_T and L_n are the temperature and density gradient scale lengths, respectively, T_i is the ion tempera-
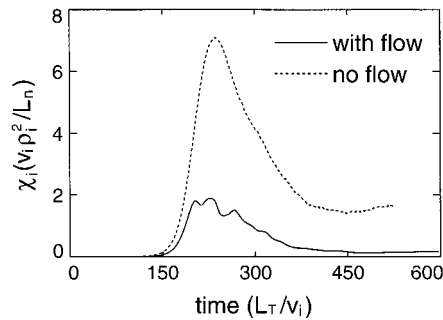

Fig. 1. Time history of ion heat conductivities with (solid) and without (dotted) $\mathbf{E} \times \mathbf{B}$ flows in global simulations with realistic plasma parameters.
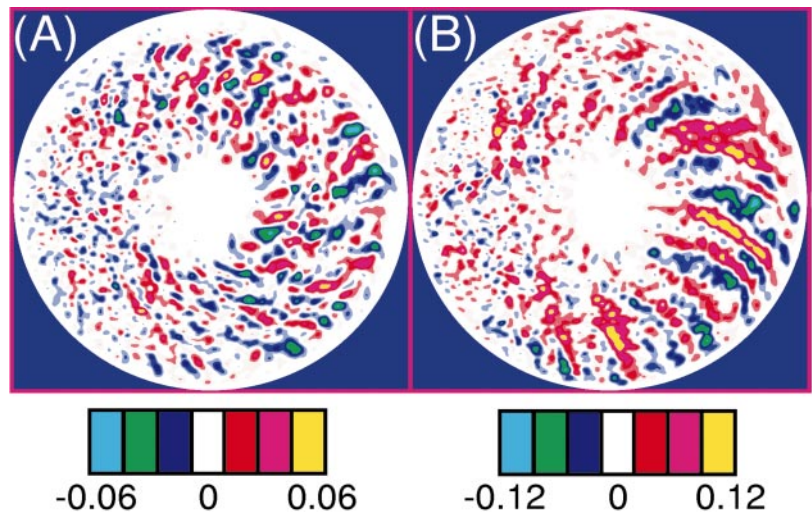

Fig. 2. Poloidal contour plots of fluctuation potential ($e\Phi/T_i$) in the steady state of nonlinear global simulation with $\mathbf{E} \times \mathbf{B}$ flows included (**A**) and with the flows suppressed (**B**). The dominant poloidal spectrum $k_\theta = 0$ mode is filtered out to highlight the differences in the turbulent eddy size.

ture, and T_e is the electron temperature. The size of the plasma column was $a = 160\rho_i$, where ρ_i is the thermal ion gyroradius measured at $r = 0.5a$. ITG modes are unstable with these parameters. The simplified physics model included a parabolic safety factor q profile, a circular cross section, no impurities, and an electron density response with $\delta n_e/n_0 = e(\Phi - \langle\Phi\rangle)/T_e$, where δn_e represents the perturbed electron density, n_0 represents the equilibrium density, $-e$ represents the electron charge, Φ represents the potential, and $\langle\Phi\rangle$ represents the flux surface averaged potential. In a typical nonlinear simulation, we calculated 5000 time steps of the trajectories of 100 million guiding centers interacting with the self-consistent turbulent field, which was discretized by 25 million grid points in a three-dimensional configuration. The instabilities evolved from a linear phase of growth to a nonlinear saturation with a peak transport level and finally to a fully developed turbulence with a steady-state transport level that is insensitive to initial conditions (Fig. 1). To illustrate the effects of these flows on transport, we also carried out simulations of the same set of parameters with $\mathbf{E} \times \mathbf{B}$ flows suppressed by forcing $\langle\Phi\rangle = 0$. Comparison of the time history of χ_i from the simulation with turbulence-driven $\mathbf{E} \times \mathbf{B}$ flows included with that from the simulation with the flows suppressed shows that a substantial reduction (up to an order of magnitude) of steady-state χ_i occurs when $\mathbf{E} \times \mathbf{B}$ flows are retained.

A key mechanism of reducing transport by $\mathbf{E} \times \mathbf{B}$ flows is the breaking of turbulent eddies and, consequently, the reduction of the radial decorrelation length (2). This process is visualized in a comparison of the poloidal contour plots of the fluctuation potential in the nonlinear phase from the broad pressure profile simulation carried out with $\mathbf{E} \times \mathbf{B}$ flows included with the one with the flows suppressed (Fig. 2). In both cases, the amplitude of fluctuations is highest at larger major radii where the drive of instabilities is strongest. Similar structures are observed in the linear phase for both cases. $\mathbf{E} \times \mathbf{B}$ flows, which are linearly stable, are generated in the

nonlinear saturation stage and begin to tear the turbulent eddies apart. In steady state, the fluctuations are observed to be nearly isotropic in radial and poloidal directions when $\mathbf{E} \times \mathbf{B}$ flows are included in the simulations, whereas the turbulent eddies are elongated along the radial direction when the flows are suppressed (Fig. 2). The fact that the breaking of turbulent eddies by $\mathbf{E} \times \mathbf{B}$ flows results predominantly in the reduction of the radial correlation length is also reflected in the observed flow-induced broadening of the radial spectrum (k_r) of fluctuations. These trends are in qualitative agreement with theoretical predictions (2, 3). We also observed that this flow-induced broadening of the k_r spectrum is accompanied by a reduction in fluctuation level, although we have not studied the relation between them in detail. Finally, the $\mathbf{E} \times \mathbf{B}$ flows also broaden the oscillation frequency of individual modes, which would otherwise have a coherent mode history corresponding to a frequency spectrum with a well-defined peak.

Fluctuating flows with a radial characteristic length comparable to that of the ambient turbulence have been generated in flux-tube simulations (8, 10). On the other hand, $\mathbf{E} \times \mathbf{B}$ flows with scale lengths of the system size have been the dominant feature in previous global gyrokinetic simulations (12, 13), although the finer scale flows began to appear in a larger system size (13). In addition, global codes typically yield a much lower value of χ_i than that from flux-tube codes. These fundamentally different trends have been attributed to differences between global and local simulation models. Specifically, the whole plasma volume is simulated in global codes with pressure gradient profile variation and fixed boundary conditions, whereas local codes have a simulation domain that covers a few turbulent decorrelation lengths with a uniform pressure gradient and use radially periodic boundary conditions.

We carried out simulations using both global and annular geometry with a variety of boundary conditions to address these differences. The perturbed electrostatic potential was set to zero at the boundary in all global simulations, and a radially periodic boundary condition similar to that of the flux-tube simulations (8, 10) was implemented in the annulus simulations. The profile of the pressure gradient was varied in the global simulations to distinguish the effects of profile variations from those of boundary conditions. When the profile of the pressure gradient was broad in global simulations, the fine-scale components of $\mathbf{E} \times \mathbf{B}$ flows with radial characteristic scale length comparable to the turbulence decorrelation length became dominant. Similar structures of the $\mathbf{E} \times \mathbf{B}$ flow shearing parameter $\omega_E \equiv dv_{E \times B}/dr$ were observed

from both the present global and local simulations (Fig. 3). Furthermore, good agreement in the ion heat conductivities was obtained between the local and global simulations with a broad pressure gradient profile. These results indicate that the radially periodic boundary conditions in local codes are not responsible for the differences between the trends observed in local and global simulations—at least for the cases studied. As the variation in the pressure gradient becomes stronger in the global simulation, a static single-well structure in the radial electric field, similar to those observed in previous global codes (12, 13), emerges and becomes dominant. At the same time, the ion heat conductivities decrease because of the profile variation effects. We conclude that the narrow pressure gradient profile in global codes is responsible for the differences with the local code results.

References and Notes

1. K. H. Burrell, *Phys. Plasmas* **4**, 1499 (1997); E. Mazzucato *et al.*, *Phys. Rev. Lett.* **77**, 3145 (1996); E. J. Synakowski *et al.*, *ibid.* **78**, 2972 (1997); H. Shirai *et al.*, *Phys. Plasmas* **5**, 1712 (1998); G. Wang *et al.*, *ibid.*, p. 1328.
2. H. Biglari, P. H. Diamond, P. W. Terry, *Phys. Fluids B* **2**, 1 (1990).
3. T. S. Hahm and K. H. Burrell, *Phys. Plasmas* **2**, 1648 (1995).
4. R. E. Bell, F. M. Levinton, S. H. Batha, E. J. Synakowski, M. C. Zarnstorff, *Plasma Phys. Control. Fusion* **40**, 609 (1998); R. J. Groebner, *Phys. Fluids B* **5**, 2343 (1993).
5. W. W. Lee, *Phys. Fluids* **26**, 556 (1983).
6. A. M. Dimits and W. W. Lee, *J. Comput. Phys.* **107**, 309 (1993); S. E. Parker and W. W. Lee, *Phys. Fluids B* **5**, 77 (1993); G. Hu and J. A. Krommes, *Phys. Plasmas* **1**, 863 (1994).
7. Z. Lin, T. S. Hahm, W. W. Lee, W. M. Tang, R. B. White, in preparation.
8. G. W. Hammett *et al.*, *Plasma Phys. Control. Fusion* **35**, 973 (1993); M. A. Beer, thesis, Princeton University, Princeton, NJ (1995).
9. R. E. Waltz, G. D. Kerbel, J. Milovich, *Phys. Plasmas* **1**, 2229 (1994).
10. A. M. Dimits, T. J. Williams, J. A. Byers, B. I. Cohen, *Phys. Rev. Lett.* **77**, 71 (1996).
11. S. E. Parker, W. W. Lee, R. A. Santoro, *ibid.* **71**, 2042 (1993).
12. J. C. Cummings, thesis, Princeton University, Princeton, NJ (1995).
13. R. D. Sydora, V. K. Decyk, J. M. Dawson, *Plasma Phys. Control. Fusion* **38**, A281 (1996).
14. Z. Lin and W. W. Lee, *Phys. Rev. E* **52**, 5646 (1995).
15. R. B. White and M. S. Chance, *Phys. Fluids* **27**, 2455 (1984).
16. A. H. Boozer, *ibid.* **24**, 1999 (1981).
17. Z. Lin, W. M. Tang, W. W. Lee, *Phys. Rev. Lett.* **78**, 456 (1997).
18. M. N. Rosenbluth and F. L. Hinton, *ibid.* **80**, 724 (1998).
19. T. S. Hahm, *Phys. Fluids* **31**, 2670 (1988); E. A. Freeman and L. Chen, *ibid.* **25**, 502 (1982).
20. T. H. Stix, *ibid.* **16**, 1260 (1973).
21. N. Winsor, J. L. Johnson, J. M. Dawson, *ibid.* **11**, 2448 (1968).
22. P. H. Diamond and Y. B. Kim, *Phys. Fluids B* **3**, 1626 (1991).
23. A. Hasegawa and M. Wakatani, *Phys. Rev. Lett.* **59**, 1581 (1987).
24. Supported by U.S. Department of Energy contract DE-AC02-76CH03073.

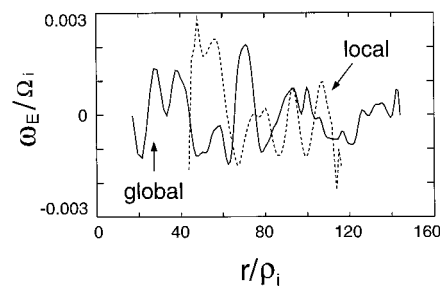20 May 1998; accepted 29 July 1998

Fig. 3. Instantaneous radial profile of $\mathbf{E} \times \mathbf{B}$ shear normalized to gyrofrequency (Ω_i) in local (dotted) and global (solid) simulations with broad profile.